Desalination and Water Treatment
www.deswater.com

doi: 10.5004/dwt.2018.23235

136 (2018) 39–48
December

Permeate flux enhancement with roughened-surface flow channel in air-gap membrane distillation systems

Chii-Dong Ho[a,*], Luke Chen[b], Chun-Hsuan Cheng[a], Tze-Hao Hsu[a], Jun-Wei Lim[c]

[a]*Energy and Opto-Electronic Materials Research Center, Department of Chemical and Materials Engineering, Tamkang University, Tamsui, New Taipei 251, Taiwan, Tel. +886 2 26215656; Fax:+886 2 26209887; emails: cdho@mail.tku.edu.tw (C.-D. Ho), 601400574@s01.tku.edu.tw (C.-H. Cheng), s8900511@gmail.com (T.-H. Hsu)*
[b]*Department of Water Resources and Environmental Engineering, Tamkang University, Tamsui, New Taipei 251, Taiwan; email: luke@mail.tku.edu.tw*
[c]*Department of Fundamental and Applied Sciences, Universiti Teknologi PETRONAS, 32610 Seri Iskandar, Perak Darul Ridzuan, Malaysia; email: junwei.lim@utp.edu.my*

Received 10 April 2018; Accepted 28 September 2018

ABSTRACT

A new design of the air-gap membrane distillation (AGMD) system for saline water desalination fabricating roughened-surface flow channel for heat transfer enhancement to produce high-purity water was investigated theoretically and experimentally. The theoretical predictions demonstrate that the AGMD system with roughened surface on the flow channel accomplishes a better device performance in pure water productivity compared with smooth-surface flow channel. The roughened-surface channel was fabricated using siphoned blasting with aluminum oxide (Al_2O_3) sand grains and arc spraying for Ni-film coating. The effect of the relative roughness was correlated with experimental data to estimate the heat transfer coefficients. A theoretical model considering both heat and mass transfer mechanisms has been developed and solved numerically. The theoretical model predicts the permeate flux increased with the inlet volumetric flow rates, inlet saline temperatures and the channel roughness. The qualitative and quantitative agreements were found between the numerical predictions and the experimental results, and the model was validated with the error analysis and the precision index of an individual measurement with the inlet temperature of hot fluid, volumetric flow rate and relative roughness as parameters. An 11% permeate flux enhancement was found when using roughened-surface flow channel of the AGMD system according to the experimental data. The effect of fabricating roughened-surface flow channel on the permeate flux and energy efficiency was also evaluated. Correlations of Nusselt number for the smooth channel and channels with fabricating roughened-surface flow were obtained using the experimental results and theoretical predictions. These correlations indicated that the flow channel using larger relative roughness gives the higher permeate flux and energy efficiency than that in the smooth-surface flow channel.

Keywords: Air-gap membrane distillation; Desalination; Relative roughness; Permeate flux; Temperature polarization

1. Introduction

Membrane distillation (MD) has advantages in distillation and water treatment with high permeate efficiency and low energy consumption. In an MD desalination process, the hot salty water vaporizes at a hydrophobic membrane surface and transports through the membrane then condensed on a cold plate to yield distillated water. The driving force for the permeate passing through the membrane is the vapor pressure difference across the membrane, while the vapor pressure difference is originated from the temperature difference across the membrane [1–3]. Four types of MD are

* Corresponding author.

usually applied, namely direct contact membrane distillation (DCMD), air-gap membrane distillation (AGMD), vacuum membrane distillation (VMD) and sweep gas membrane distillation (SGMD). Among them, DCMD is suffered with the higher heat loss, VMD has the pore wetting risk and SGMD is difficult to recover heat. Although AGMD has higher heat efficiency, the system needs to improve its lower flux problem while maintaining an acceptable energy efficiency. To improve the AGMD system in this regard, the specifications of membrane material on distillation performance [4] and the effects of the feed flow rate and feed temperature were studied [5,6]. The comprehensive experimental and theoretical studies on the performance of an AGMD module were also explored to predict the pure water productivity [7–9]. Integration of solar heat as heat source with AGMD system such as immediate assisted solar AGMD system was also investigated [10,11].

AGMD is best suited for pure water productivity where water vapor is the major permeate component [12]. Reduction of the temperature polarization effect was achieved using eddy promoters in flow channel to enhance the device permeate flux performance of MD operations in previous theoretical and experimental studies [13] and computational simulation [11,14]. Comparing simulation results with experimental data, the studies confirmed that the theoretical model is capable in simulating heat and mass transfer in the MD desalination system. Previous investigation in improving the flux enhancement with inserting filament into the flow channel of DCMD modules to promoting the turbulence [15], this study is a new design of a cheaper and easier fabrication for creating turbulent flow, or eddy promoter, with fabricating roughened-surface flow channel of AGMD modules. The objective of this study is to fabricate roughened-surface flow channel into an improved flat plate AGMD modules for reducing its temperature polarization and to enhance the device permeate flux performance while keeping acceptable energy efficiency. A theoretical model was also developed for predicting the pure water productivity and was validated with the experimental data.

2. Mathematical modeling of the AGMD system

For AGMD system, a theoretical model considering both heat and mass transfer mechanisms to model how hot liquid water was vaporized, then transported through porous hydrophobic membranes and condensed on the cold side plate. The mass transfer occurs in the porous membrane and air gap while the heat transfer takes place in the domains including the hot feed, membrane, air gap, cooling plate, and cold fluid of the distillation process, as shown in Fig. 1. Because pure water productivity of AGMD desalination system was observed and conducted in our laboratory with neglected difference between concurrent and counter-current operations; therefore, only concurrent operation was considered in this study. The theoretical model is based on the following assumptions: (a) under steady-state operations; (b) physical properties of fluid, plates and membrane are constants; (c) stagnant air within the membrane pore; (d) the condensate forms a thin liquid film and covers the entire condensing surface;

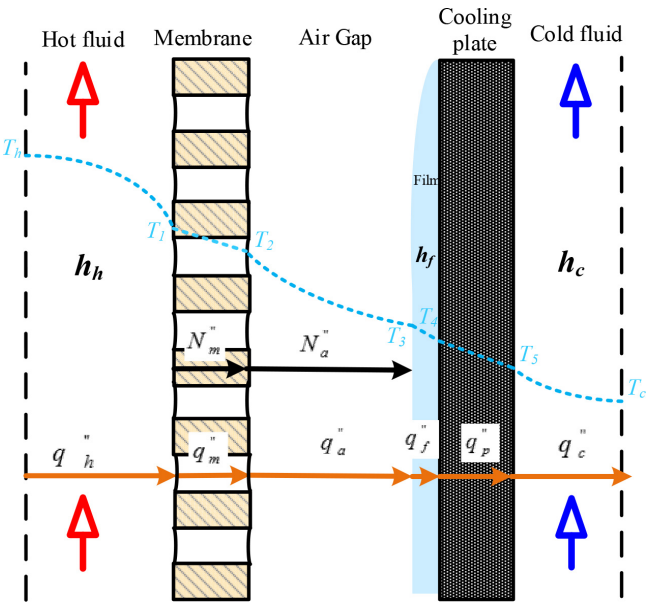

Fig. 1. Heat and mass transfer mechanisms in the AGMD module.

(e) mass transfer by diffusion and heat transfer by conduction within the air gap; (f) no water passing through the membrane; and (g) well insulation on the bottom and edge sides of modules.

2.1. Heat transfer

The permeate flux in the non-isothermal process of the AGMD module can be determined from the energy balance of enthalpy flow in different regions for (1) the hot feed stream, (2) hydrophobic membrane, (3) air gap, (4) cooling plate and (5) cooling water, and the convectional AGMD under steady-state operation may be written as follows:

In the saline water region with neglecting the net enthalpy flow due the temperature change,

$$q''_h = h_h(T_h - T_1) \tag{1}$$

At the membrane,

$$q''_m = \frac{k_m}{\delta_m}(T_1 - T_2) + N''_m\lambda \tag{2}$$

Inside the air gap,

$$q''_a = \frac{k_a}{\delta_a}(T_2 - T_3) + N''_a\lambda \tag{3}$$

In the permeate film with the heat transfer coefficient for the condensate film [16],

$$q''_f = h_f(T_3 - T_4) = 0.943\left[\frac{\rho^2 g\lambda k_f^3}{\mu L(T_3 - T_4)}\right]^{\frac{1}{4}}(T_3 - T_4) \tag{4}$$

At the condensing plate,

$$q_p'' = \frac{k_p}{\delta_p}(T_4 - T_5) \tag{5}$$

In the cooling water,

$$q_c'' = h_c(T_5 - T_c) \tag{6}$$

The modeling equations among the heat fluxes for all layers and for the one-dimensional bulk fluids with assuming well insulation on the bottom and edge sides of modules give as follows:

$$q_h'' = q_m'' = q_a'' = q_f'' = q_p'' = q_c'' \tag{7}$$

The longitudinal temperature distributions for hot and cold side channels were related with heat and mass fluxes that pass through the membrane as equations below:

$$\frac{dT_h}{dz} = \frac{-Wq_h''}{\dot{m}C_{p,h}} \tag{8}$$

$$\frac{dT_c}{dz} = \frac{Wq_c''}{\dot{m}C_{p,c}} \tag{9}$$

2.2. Mass transfer

The mass transfer flux is modeled by the mass transfer resistances in series of both the membrane and air gap with neglecting the resistances in other layers. The permeate flux of water vapor was incorporating with a membrane permeation coefficient [16] to estimate the amount of permeate flux that passes through the membrane pores as follows:

$$N_m^{"} = c_m \Delta P = c_m(P_1^{\text{sat}} - P_2^{\text{sat}}) \tag{10}$$

where P_1^{sat} and P_2^{sat} are the saturated pressure of water vapor on the membrane surfaces in hot saline stream and the air gap calculated using Eqs. (12) and (13), and the total saturated pressure of the mixtures P_w^{sat} is calculated with the Antoine equation. The permeate flux diffuses through the air gap and reaches to the cooling plate, then was condensed as the collected water. For the effect of the non-volatile solute with lower saturation vapor pressure, the water activity coefficient a_w was calculating using the correlation below [17]:

$$a_w = 1 - 0.5x_{\text{NaCl}} - 10x_{\text{NaCl}}^2 \tag{11}$$

$$P_1^{\text{sat}} = x_w a_w P_w^{\text{sat}} \tag{12}$$

$$P_2^{\text{sat}} = y_w a_w P_w^{\text{sat}} \tag{13}$$

In which, y_w and x_w are the vapor and water molar fractions, respectively. The amount of the molar vapor flux diffusing through a stagnant air film over the air gap layer by molecular diffusion [17] was expressed as follows:

$$N_a^{"} = c_a(P_2^{\text{sat}} - P_3^{\text{sat}}) \tag{14}$$

The overall vapor flux was calculated by equating the permeate fluxes in the membrane and air gap (Eqs. (2) and (3)) with the total mass-transfer resistances:

$$N_a'' = N_m'' = N'' = c_T(P_1^{\text{sat}} - P_3^{\text{sat}}) \tag{15}$$

$$c_T = \left(\frac{1}{c_m} + \frac{1}{c_a}\right)^{-1} \tag{16}$$

The combinations of each heat flux term of Eqs. (2)–(6) lead to obtain the overall heat transfer coefficient of the hot stream and cooling stream, respectively.

$$\begin{aligned} q_{ma}'' &= q_a'' + q_m'' \\ &= \left\{\left(\frac{k_m}{\delta_m} + \frac{k_a}{\delta_a}\right)^{-1} \right. \\ &\quad \left. + \left[c_T \frac{((1-x_{\text{NaCl}})(1-0.5x_{\text{NaCl}} - 10x_{\text{NaCl}}^2)P_w^{\text{sat}} + P_3^{\text{sat}})\lambda^2 M_w}{2RT_{\text{avg}}^2}\right]\right\} \\ &\quad \times (T_1 - T_3) = H_m(T_1 - T_3) \end{aligned} \tag{17}$$

$$\begin{aligned} q_{fc}'' &= q_f'' + q_p'' + q_c'' \\ &= \frac{1}{\frac{1}{h_f} + \frac{\delta_p}{k_p} + \frac{1}{h_c}}(T_3 - T_c) = H_c(T_3 - T_c) \end{aligned} \tag{18}$$

Manipulating and solving Eqs. (17) and (18) with the aid of Eq. (1) lead to the following:

$$T_h = T_1 + \frac{H_m}{h_h}(T_1 - T_3) \tag{19a}$$

$$T_c = T_3 + \frac{H_m}{H_c}(T_1 - T_3) \tag{19b}$$

or

$$T_1 = \frac{h_h T_h + H_m T_3}{h_h + H_m} \tag{20a}$$

$$T_3 = \frac{H_c T_c + H_m T_1}{H_c + H_m} \tag{20b}$$

Eq. (19b) is subtracted from Eq. (19a) to give the following:

$$\tau_{\text{temp}} = \frac{h_h H_c}{h_h H_c + h_h H_m + H_c H_m} \tag{21}$$

Combination of Eqs. (8) and (9) with Eq. (21) gives the following:

$$\frac{dT_h}{dz} = \frac{-W}{\dot{m}_h C_{p,h}} H_m \tau_{\text{temp.}} (T_h - T_c) \tag{22}$$

$$\frac{dT_c}{dz} = \frac{W}{\dot{m}_c C_{p,c}} H_m \tau_{\text{temp.}} (T_h - T_c) \tag{23}$$

3. Experimental setup

The schematic representation of the AGMD module is illustrated in Fig. 2. The details of the AGMD module with the roughened-surface channels of hot and cold streams are illustrated in Fig. 3, respectively. The outside walls of the entire module are acrylic plates while the roughened-surface aluminum plate fabricated by siphonic-blasting was embedding into the hot side acrylic channel plate and serving as turbulence promoters. The acrylic plate has three holes for the fluid distribution flowing in and out at both the entrance and exit ends, respectively. The dimensions of the hot and cold channels are 0.21 m in length, 0.29 m in width, and 2 mm in height, respectively. The hydrophobic polytetrafluoroethylene membrane (ADVANTEC) with a nominal pore size of 0.1 μm, a porosity of 0.72, and a thickness of 130 μm was used. The experiments were conducted for various inlet hot fluid temperatures (40°C, 45°C, 50°C, 55°C) with four flow rates (0.3, 0.5, 0.7, 0.9 L/min) and two inlet cold fluid temperatures (15°C, 25°C). The wound grid of nylon fibers with 0.2 mm of diameter inserted between the silicon rubber and membrane surface to prevent from membrane bending and wrinkling in the hot stream channel while the 1mm-thick carbon-fiber sheet was implemented as a support in the air-gap channel. Between the roughened surface and aluminum plate or the acrylic plate is a 1 mm-thick silicon rubber sealing to create channels and to prevent leakage. Because the vertical support sheet occupied 13% of the entire membrane flux area, its effect in preventing permeate flux is considered in calculating net flux area of the membrane. The permeate flux reached and condensed at the thin aluminum plate, which was collected and weighted using an electronic balance. Because the dimension of the air gap is 2 mm which is less than 5 mm, the convection inside the gap can be neglected [18].

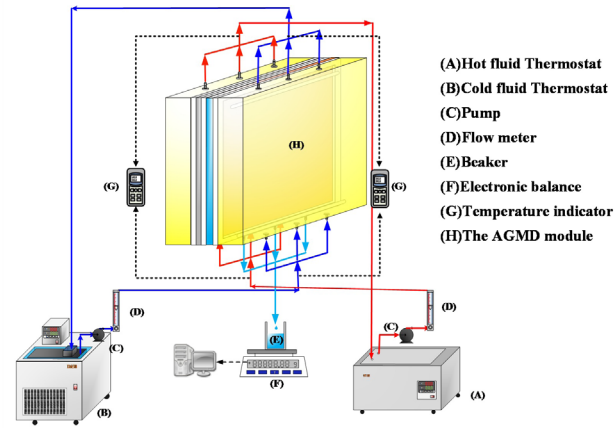

Fig. 2. Experimental setup of the AGMD system.

4. The numerical calculation

Assume the convective heat-transfer coefficients (h_h) with given experimental mass flux N_{exp}'', the temperature on both sides of membrane surfaces (T_1 and T_3) were calculated by Eqs. (19) and (20) with inlet and outlet temperatures of both hot and cold streams were known. The calculated values of the convective heat-transfer coefficients and the temperatures of both membrane surfaces were conveyed to the left-hand side of Eqs. (22) and (23) to solve the temperatures of both hot and cold streams in Eqs. (22) and (23) by using the fourth-order Runge–Kutta method along the longitudinal direction of the AGMD module. An iteration procedure was performed to determine the convective heat-transfer coefficients h_h, the temperature on the membrane surfaces (T_1 and T_3) with 0.1% error as accuracy control.

The correlation between the heat transfer coefficients of roughened-surface channel used in the channel of hot feed stream with that of laminar flow in smooth-surface channel is proposed as follows:

$$Nu^T = \frac{d_{h,h} h_h}{k} = \alpha^T Nu_{\text{lam}} \tag{24}$$

where α^T is the corrected factor and depends on the turbulent intensity created by the relative roughness of flow conduit. The Buckingham's π theorem was performed to derive a simple expression of Nusselt numbers in the roughened-surface flow channel as follows:

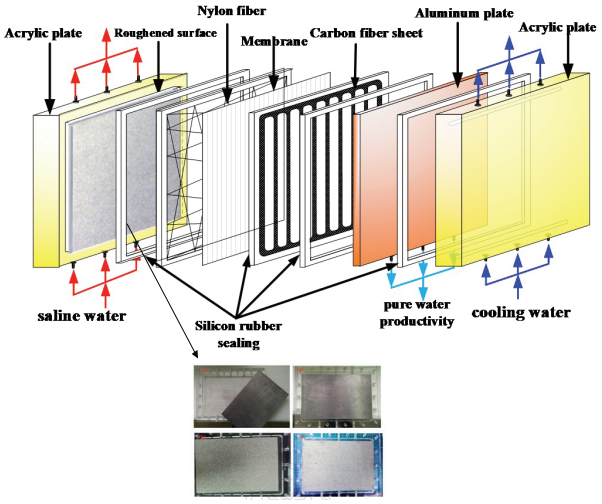

Fig. 3. Fabrication structure of the AGMD module and pictures of the roughened surfaces.

$$\alpha^T = \frac{Nu^T}{Nu_{\text{lam}}} = f\left(\frac{\varepsilon_r}{d_{h,h}}\right) \tag{25}$$

where $\varepsilon_r/d_{h,h}$ stands for a relative roughness which was used as a correlation factor to regress with heat transfer coefficients h_h to obtain a polynomial regression equation as shown in Eq. (26):

$$\frac{Nu^T}{Nu_{\text{lam}}} = \alpha^T = f\left(\frac{\varepsilon_r}{d_{h,h}}\right) = a\left(\frac{\varepsilon_r}{d_{h,h}}\right)^2 + b\left(\frac{\varepsilon_r}{d_{h,h}}\right) + c \tag{26}$$

The coefficients in the polynomial regression equation then were obtained from curve fitting with the squared correlation coefficient ($R^2 = 0.97$), as shown in Fig. 4.

$$Nu^T = \left[-57.88\left(\frac{\varepsilon_r}{d_{h,h}}\right)^2 + 15.40\left(\frac{\varepsilon_r}{d_{h,h}}\right) + 0.89\right] Nu_{\text{lam}} \tag{27}$$

Eq. (27) depicts the correlation factor between the turbulent heat transfer enhanced by using the roughened surface and the laminar heat transfer without roughened surface. Where, the Nusselt number of laminar flow in smooth-surface channel was derived by Phattaranawik and Jiraratananon [15].

$$Nu_{\text{lam}} = 4.36 + \frac{0.036\,\text{Re}\,\text{Pr}\left(De/L\right)}{1 + 0.011\left(\text{Re}\,\text{Pr}\left(De/L\right)\right)^{0.8}} \tag{28}$$

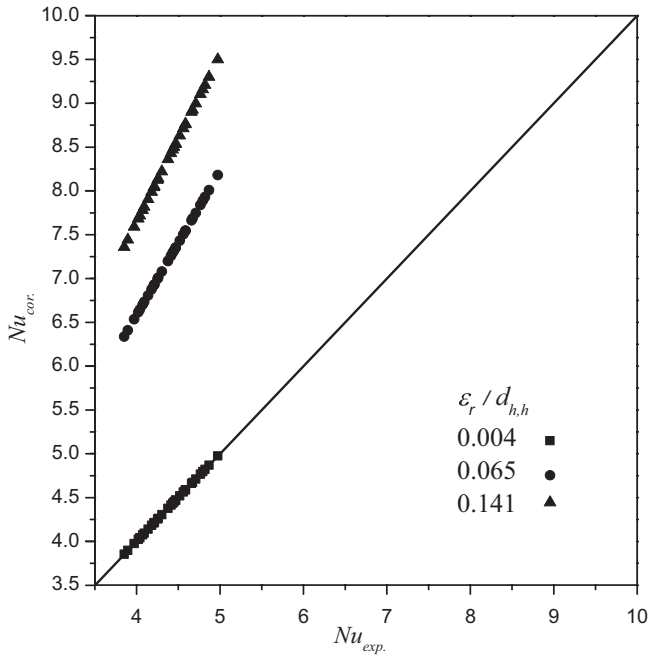

Fig. 4. Comparisons of correlated and experimental Nusselt numbers.

The increment of energy consumption is inevitable due to utilizing the roughened-surface flow channel. The energy consumption of the AGMD module includes the energy required for both the hot and cold fluid sides. They are determined by using Fanning friction factor f_F and the corresponding flows and channel dimensions as follows [19]:

$$P_{\text{lost}} = P_h + P_c = \dot{m}_h \ell w_{f,h} + \dot{m}_c \ell w_{f,c} = Q_h \rho_h \ell w_{f,h} + Q_c \rho_c \ell w_{f,c} \tag{29}$$

$$\ell w_{f,h} = \frac{2 f_{F,h} u_h^2 L}{d_{h,h}}, \qquad \ell w_{f,c} = \frac{2 f_{F,c} u_c^2 L}{d_{h,c}} \tag{30}$$

in which,

$$d_{h,h} = \frac{4((D-\varepsilon_r)W)}{2((D-\varepsilon_r)+W)}, \qquad d_{h,c} = \frac{4DW}{2(D+W)} \tag{31}$$

$$u_h = \frac{Q_h}{(D-\varepsilon_r)W}, \qquad u_c = \frac{Q_c}{DW} \tag{32}$$

The Fanning friction factor was estimated by using a correlation based on the aspect ratio of the channel ($\alpha = D/W$) [20]:

$$f_{F,h} = \frac{C}{\text{Re}_h}, \quad f_{F,c} = \frac{C}{\text{Re}_c}, \quad \text{Re}_h = \frac{\rho_h u_h d_{h,h}}{\mu_h}, \quad \text{Re}_c = \frac{\rho_c u_c d_{h,c}}{\mu_c} \tag{33}$$

$$C = 24(1 - 1.3553\alpha + 1.9467\alpha^2 - 1.7012\alpha^3 + 0.9564\alpha^4 - 0.2537\alpha^5) \tag{34}$$

The variation of flow rates also reflects the change in flow velocity calculated by Eq. (32), and the residence time of feed fluid lumped in the Reynolds number in Eq. (33).

To evaluate the energy increment with the corresponding flux enhancement, the ratio of flux enhancement and power consumption increment, I_N and I_P, is defined, respectively, as follows:

$$I_N = \frac{N_s'' - N_n''}{N_n''} \tag{35}$$

$$I_p = \frac{P_s - P_n}{P_n} \tag{36}$$

where the subscripts s and n represent the channels with roughened-surface flow channel and the empty channels. The values of the parameters and the correlated equations used in the numerical prediction are all listed in Table 1.

5. Results and discussion

The permeate flux is dependent on the temperature gradient between the membrane surface, namely T_1 and T_3,

Table 1
The parameter values or correlated equations used in the numerical prediction

Values or correlated equations	Unit
$c_m = \left\{ \left[1.064 \frac{\varepsilon r}{\tau \delta_m} \left(\frac{M_W}{RT_m} \right)^{1/2} \right]^{-1} + \left[\frac{1}{\lvert Y_m \rvert_{\ln}} \frac{D_m \varepsilon}{\delta_m \tau} \frac{M_w}{RT_m} \right]^{-1} \right\}^{-1}$	$\frac{kg}{m^2\ Pa\ hr}$
$c_a = \frac{1}{\lvert Y_a \rvert_{\ln}} \frac{D_a}{\delta_a} \frac{M_W}{RT_a}$	$\frac{kg}{m^2\ Pa\ hr}$
$c_T = \left\{ \left[1.064 \frac{\varepsilon r}{\tau \delta_m} \left(\frac{M_W}{RT_m} \right)^{1/2} \right]^{-1} + \left[\frac{1}{\lvert Y_m \rvert_{\ln}} \frac{D_m \varepsilon}{\delta_m \tau} \frac{M_w}{RT_m} \right]^{-1} + \left[\frac{1}{\lvert Y_a \rvert_{\ln}} \frac{D_a}{\delta_a} \frac{M_w}{RT_a} \right]^{-1} \right\}^{-1}$	$\frac{kg}{m^2\ Pa\ hr}$
$\delta_a = 0.002$	m
$\delta_m = 130$	μm
$\delta_p = 0.01$	m
$Cp_h = 4144.4574 - 241.35681m + 16.47156m^2$	$\frac{J}{kg\ \mathrm{k}}$
$Cp_c = 1000 \begin{pmatrix} 6.18507 - 0.0159(T + 273.15) + 3.99 \times 10^{-5} (T + 273.15)^2 \\ -3.06 \times 10^{-8} (T + 273.15)^3 \end{pmatrix}$	$\frac{J}{kg\ \mathrm{k}}$
$\tau_{\text{temp}} = \frac{T_1 - T_3}{T_h - T_c}$	–
$k_a = 0.0144 - 2.16 \times 10^{-5} (T + 273.15) + 1.32 \times 10^{-7} (T + 273.15)^2$	$\frac{W}{m\ \mathrm{K}}$

in the AGMD system. Operation parameters such as the hot and cold inlet temperatures, volumetric flow rate, and channel roughness may affect the longitudinal temperature profile of the channel in the AGMD module. They then also affect the permeate flux in the AGMD system. The effect of the relative roughness on the temperature profiles inside the AGMD modules is shown in Fig. 5. When comparing the temperature profiles of the relative channel roughness 0.004 and 0.141, one finds the higher roughness results in more temperature gradient between the membrane surface (T_1 and $T_{3)}$. This is due to the well mixed in the bulk flow of the roughen channel that makes the bulk flow temperature approximate to the temperature of the hot side of the membrane (T_1), hence enlarge the gradient between membrane surface temperature T_1 and T_3.

The permeate flux increases with the increasing inlet hot flow rate is due to the convective heat-transfer coefficient enhancement in the hot feed stream, and thus, the thinner thermal boundary layer with a lower thermal resistance results in a higher heat transfer, and also results in higher mass transfer as shown in Fig. 6. Similar results were also found in previous study of desalination with polyethylene membrane [21]. Reduction of thermal boundary layer thickness could increase vapor pressure gradient, which results in a higher permeate flux through the hydrophobic membrane. That is, the results that the permeate flux increases with increasing the inlet hot fluid temperature, and flow rate are consistent

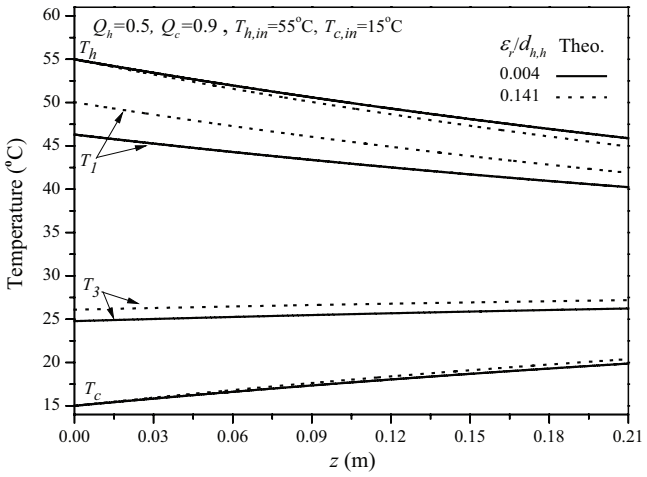

Fig. 5. Effect of relative roughness on temperature profiles.

with parameters analyses in AGMD simulation study [22]. The degree of permeate flux enhancement increases with the inlet hot fluid temperature and relative roughness was confirmed by Table 2. The maximum permeate flux enhancement (I_N) in operating the roughened-surface flow channel can be up to 11% increase relative to the cases of smooth flow channel ($\varepsilon_r/d_{h,h}$ = 0.004).

The permeate fluxes were calculated through the heat transfer coefficient correction factor (Eq. (27)) for predicting the Nusselt number in roughened-surface flow channel, as referred to the heat transfer efficiency. The agreement between the experimental results and theoretical predictions of permeate flux for various hot feed flow rates under different inlet temperature and channel roughness is elicited in Fig. 7. The agreement convinces that the proposed theoretical model is a reliable model for permeate flux prediction in the AGMD module system. Noticed that the larger the relative channel roughness, the more the feed rate and the higher temperature result in the more permeate flux. A considerable permeate flux enhancement by using roughened surface caused turbulent intensity was found when comparing the permeate flux enhancement between the relative roughness of 0.004 and 0.065, while less permeate flux increment was found as the relative roughness increased from 0.065 to 0.141. Although the larger relative roughness induces more turbulence that enhances more permeate flux, the larger relative roughness also causes more energy consumption as well. Therefore, an optimal relative roughness must be assessed when both permeate flux enhancement and energy consumption increment are considered as discussed in the following. Considerations of both permeate flux productivity and hydraulic dissipation

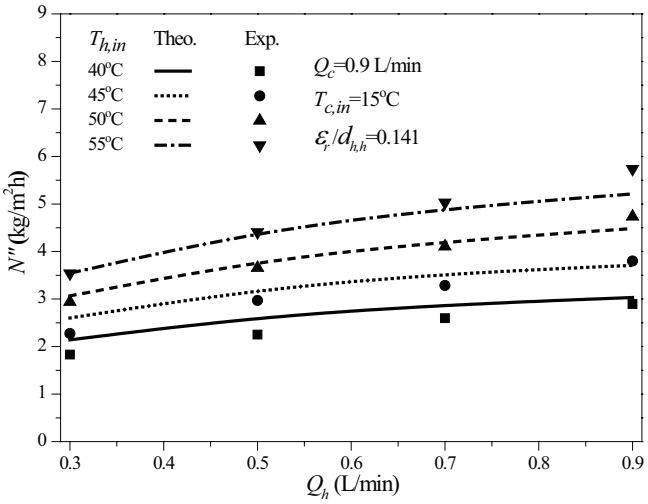

Fig. 6. Effects of saline inlet temperature and volumetric flow rate of on permeate fluxes.

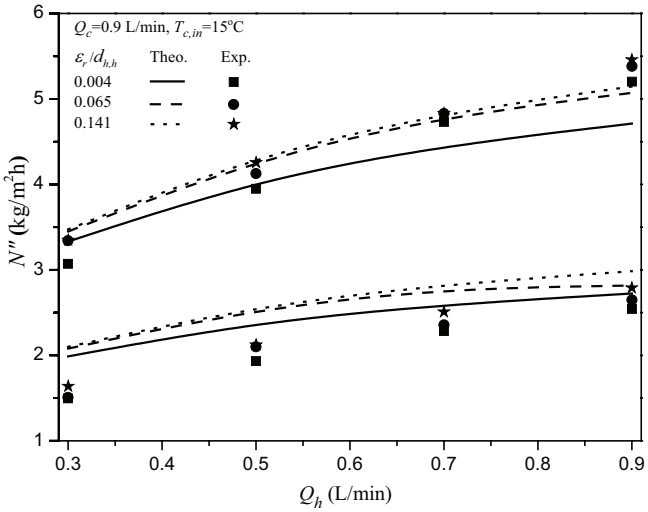

Fig. 7. Effects of hot saline inlet temperature, volumetric flow rate and relative roughness on permeate fluxes.

Table 2
Comparisons of numerical and experimental results of permeate fluxes for the AGMD modules

$T_{c,in}$ = 15°C	Q_c = 0.9 L/min	Saline water, NaCl = 3.5 wt%				
		Relative roughness $\varepsilon_r/d_{h,h}$				
$T_{h,in}$ (°C)	Q_h (L/min)	0.004	0.065		0.141	
		N''_{Theo} (kg/m^2 h)	N''_{Theo} (kg/m^2 h)	I_N (%)	N''_{Theo} (kg/m^2 h)	I_N (%)
40	0.3	1.988	2.08	4.6	2.1	5.6
	0.5	2.388	2.546	6.6	2.578	8.0
	0.7	2.593	2.783	7.3	2.83	9.1
	0.9	2.724	2.817	3.4	2.985	9.6
45	0.3	2.418	2.529	4.6	2.553	5.6
	0.5	2.92	3.116	6.7	3.162	8.3
	0.7	3.191	3.431	7.5	3.527	10.5
	0.9	3.315	3.625	9.4	3.68	11.0
50	0.3	2.879	3.001	4.2	3.015	4.7
	0.5	3.483	3.71	6.5	3.753	7.8
	0.7	3.821	4.091	7.1	4.157	8.8
	0.9	4.038	4.334	7.3	4.398	8.9
55	0.3	3.332	3.45	3.5	3.475	4.3
	0.5	4.051	4.301	6.2	4.344	7.2
	0.7	4.456	4.796	7.6	4.837	8.6
	0.9	4.713	5.073	7.6	5.147	9.2

caused energy consumption increase are compared graphically in Fig. 8, and the data are listed in Table 3 in terms of I_N/I_P ratio with inlet saline temperature, volumetric flow rate, and relative roughness as parameters. The increase of inlet saline temperature gives higher value of I_N/I_P, which means the expenses of energy consumption is more effective in increasing the permeate flux. In other words, the percentage of permeate flux enhancement is higher than that of energy consumption increment but it decrease with increasing the volumetric flow rate. Comparing the effect of relative roughness ($\varepsilon_r/d_{h,h}$ = 0.141 vs. 0.065) with inlet saline temperature (55°C vs. 40°C) on I_N/I_P ratio in Fig. 8, one finds that the relative roughness has more profound effect on the I_N/I_P ratio than the inlet saline temperature. The effective utilization of power consumption in producing pure water with the AGMD module, in terms of I_N/I_P, was found when $\varepsilon_r/d_{h,h}$ = 0.141 relative roughness is used.

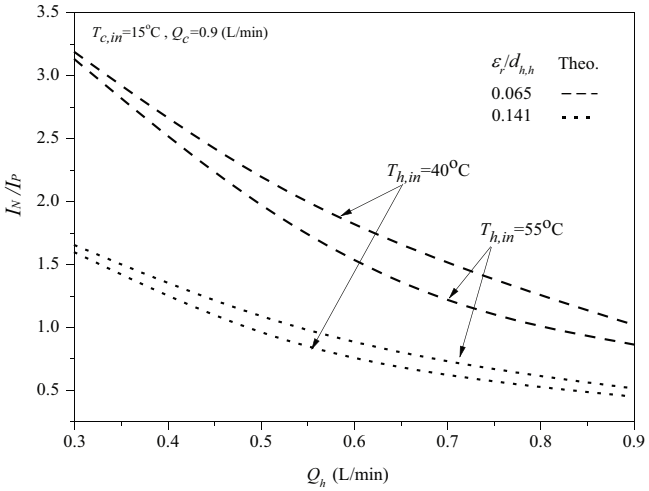

Fig. 8. Effects of saline inlet temperature and relative roughness on I_N/I_P.

Table 3
Effects of operation conditions and relative roughness on the I_N/I_P ratio

$T_{c,in}$ (°C)	$T_{h,in}$ (°C)	Q_h (L/min)	Pure water test		Saline water, NaCl = 3.5 wt%	
			I_N/I_P			
			Relative roughness $\varepsilon_r/d_{h,h}$			
			0.065	0.141	0.065	0.141
25	40	0.3	2.424	1.200	2.420	1.232
		0.5	1.392	0.693	1.436	0.767
		0.7	0.920	0.443	0.920	0.489
		0.9	0.667	0.334	0.688	0.377
	55	0.3	2.406	1.210	2.476	1.254
		0.5	1.527	0.760	1.583	0.797
		0.7	1.086	0.523	1.112	0.573
		0.9	0.799	0.394	0.824	0.414
15	40	0.3	3.285	1.629	3.128	1.595
		0.5	1.799	0.892	1.893	0.895
		0.7	1.126	0.563	1.139	0.598
		0.9	0.798	0.408	0.864	0.450
	55	0.3	3.636	1.686	3.186	1.653
		0.5	2.007	1.002	2.128	1.045
		0.7	1.355	0.667	1.487	0.708
		0.9	1.029	0.492	1.020	0.515

6. Conclusions

The roughened-surface flow channel in AGMD system was implemented and developed theoretically considering both the heat and mass transfer of each layer of the AGMD modules and validated by experimental data. The developed numerical model was used in predicting temperature distributions and pure water productivity with inlet saline temperature, the volumetric flow rates, and relative roughness as parameters. Experimental study has demonstrated its feasibility and can be up to 11% enhancement of permeate flux by the roughened-surface AGMD system when compared with the smooth channel. The effects of the roughened-surface channel in AGMD system on the desalination performance and power consumption were also compared and evaluated. Correlations of Nusselt number for smooth channel and roughened-surface channels have been obtained using the experimental results and theoretical predictions. These correlations indicated that the relative roughness has more profound effect on the I_N/I_P ratio than the inlet saline temperature. The effective utilization of power consumption in producing pure water with the AGMD module, in terms of I_N/I_P, was found when $\varepsilon_r/d_{h,h}$ = 0.141 relative roughness is used.

Acknowledgment

The authors wish to thank the Ministry of Science and Technology of the Republic of China for its financial support.

Symbols

a_w	—	Water activity in NaCl solution
c_a	—	Membrane mass transfer coefficient of air gap, kg/(m² pa h)
c_m	—	Membrane mass transfer coefficient of membrane, kg/(m² pa h)
c_T	—	Overall mass transfer coefficient, kg/(m² pa h)
C	—	Constant defined by Eq. (34)
$C_{p,c}$	—	Heat capacity of cold fluid, J/(kg K)
$C_{p,h}$	—	Heat capacity of hot fluid, J/(kg K)
$d_{h,c}$	—	Hydraulic diameter of cold fluid, m
$d_{h,h}$	—	Hydraulic diameter of hot fluid, m
D	—	Conduit height, m
f_F	—	Fanning fraction factor
g	—	Gravitational acceleration, m/s²
h_c	—	Convection coefficient of cold fluid, W/(m² K)
h_f	—	Convection coefficient of condensation, W/(m² K)
h_h	—	Convection coefficient of hot fluid, W/(m² K)
H_c	—	Over-all heat transfer coefficient of cold fluid, W/(m² K)
H_m	—	Thermal convection coefficient of membrane, W/(m² K)
I_N	—	Permeate flux improvement, defined by Eq. (35)

I_P — Power consumption increment defined by Eq. (36)
k — Thermal conductivity coefficient of the fluid, W/m K
k_a — Thermal conductivity coefficient of air gap, W/m K
k_f — Thermal conductivity coefficient of aqueous solution, W/m K
k_m — Average thermal conductivity coefficient of membrane, W/m K
k_p — Average thermal conductivity coefficient of the cooling plate, W/m K
L — Axial distance, m
lw_f — Friction loss of conduits, J/kg
$\dot{m}$ — Mass flow rate, kg/s
M_w — Molecular weight of water vapor, kg/mol
N'' — Permeate flux, kg/(m^2 h)
N''_a — Permeate flux of the air gap, kg/(m^2 h)
N''_m — Permeate flux in the membrane, kg/(m^2 h)
N''_n — Permeate flux for the empty channels, kg/(m^2 h)
N''_s — Permeate flux for the roughened-surface flow channel, kg/(m^2 h)
Nu — Nusselt number
Nu^T — Nusselt number of the eddy promoter
P_1^{sat} — Saturated vapor pressure between the hot fluid and membrane surface, Pa
P_2^{sat} — Saturated vapor pressure between the air gap and membrane surface, Pa
P_3^{sat} — Saturated vapor pressure of the cold fluid, Pa
P_w^{sat} — Saturated vapor pressure of membrane surface, Pa
P_{lost} — Overall hydraulic loss of the hot and cold fluid, W
P_n — Hydraulic friction loss of the cold fluid on the empty channel, W
P_s — Hydraulic friction loss of the cold fluid on the roughened-surface, W
P_T — Total pressure, Pa
Pr — Prandtl number
q''_a — Heat transfer rate between condensation and air gap membrane surface, W/m^2
q''_c — Heat transfer rate between cooling plate and cold fluid, W/m^2
q''_f — Heat transfer rate between condensation and cooling plate, W/m^2
q''_h — Heat transfer rate between hot fluid and membrane surface, W/m^2
q''_m — Heat transfer rate between membrane surface of hot fluid and air gap, W/m^2
q''_p — Heat transfer rate of cooling plate, W/m^2
q''_{ma} — Total heat transfer rate of the membrane to the air gap, W/m^2
q''_{fc} — Over-all heat transfer coefficient of the condensation to the cold fluid, W/m^2
Q — Volume flow rate of fluid, m^3/s
R — Gas constant, J/mol K
Re — Reynolds number
T_1 — Temperature of hot fluid membrane surface, °C
T_2 — Temperature of air gap membrane surface, °C
T_3 — Temperature of condensation membrane surface, °C
T_4 — Temperature of cooling plate membrane surface, °C
T_5 — Temperature of cold fluid membrane surface, °C
T_c — Temperature of cold fluid, °C
T_h — Temperature of hot fluid, °C
T_{avg} — Average temperature of hot fluid membrane surface and condensation, °C
μ — Average fluid flow rate, m/s
W — Conduit width, m
x_{NaCl} — Liquid mole fraction of NaCl
x_w — Liquid mole fraction of water
y_w — Vapor mole fraction of water
z — Conduit coordinate

Greeks

α — Conduit section rate
α^{T} — Eddy promoter
ΔP — Vapor pressure difference of membrane, Pa
ε_r — Absolute roughness, m
λ — Latent heat of water, J/kg
μ — Fluid viscosity, (N s)/m2
ρ — Density of fluid, kg/m3
τ_{temp} — Temperature polarization coefficient
δ_a — Thickness of air gap, m
δ_m — Thickness of membrane, m
δ_p — Thickness of cooling plate, m

Subscripts

c — Cold fluid
h — Hot fluid
in — At the inlet
lam — Laminar flow
out — At the outlet
Cal. — Iterative calculation
Exp. — Experimental data

References

[1] O. Miyatake, H. Iwashita, Laminar-flow heat transfer to a fluid flowing axially between cylinders with a uniform wall heat flux, Int. J. Heat Mass Transfer, 8 (1991) 322–331.
[2] K.W. Lawson, D.R. Lloyd, Membrane distillation, J. Membr. Sci., 124 (1997) 1–25.
[3] K.W. Lawson, D.R. Lloyd, Membrane distillation. II. Direct contact MD, J. Membr. Sci., 120 (1996) 123–133.
[4] Y.W. Kai, T.S. Chunga, M. Gryta, Hydrophobic PVDF hollow fiber membranes with narrow pore size distribution and ultra-thin skin for the freshwater production through membrane distillation, Chem. Eng. Sci., 63 (2008) 2587–2594.
[5] A.S. Alsaadi, N. Ghaffour, J.D. Li, S. Gray, L. Francis, H. Maab, G.L. Amy, Modeling of air-gap membrane distillation process: a theoretical and experimental study, J. Membr. Sci., 445 (2013) 53–65.
[6] H. Geng, H. Wu, P. Li, Q. He, Study on a new air-gap membrane distillation module for distillation, Desalination, 334 (2014) 29–38.
[7] A. Alkhudhiri, N. Darwish, N. Hilal, Treatment of saline solutions using air gap membrane distillation: experimental study, Desalination, 323 (2013) 2–7.

[8] A.E. Khalifa, Water and air gap membrane distillation for water desalination – an experimental comparative study, Sep. Purif. Technol., 141 (2015) 276–284.
[9] A. Khalifa, D. Lawal, M. Antar, M. Khayet, Experimental and theoretical investigation on water desalination using air gap membrane distillation, Desalination, 376 (2015) 94–108.
[10] H. Chang, C.L. Chang, C.D. Ho, C.C. Li, P.H. Wang, Experimental and simulation study of an air gap membrane distillation module with solar absorption function for desalination, Desal. Wat. Treat., 25 (2011) 251–258.
[11] M. Shakaib, S.M.F. Hasani, I. Ahmed, R.M. Yunus, A CFD study on the effect of spacer orientation on temperature polarization in membrane distillation modules, Desalination, 284 (2012) 332–340.
[12] A.M. Alklaibi, N. Lior, Transport analysis of air-gap membrane distillation, J. Membr. Sci., 255 (2005) 239–253.
[13] C.D. Ho, H. Chang, C.L. Chang, C.H. Huang, Theoretical and experimental studies of performance enhancement with roughened surface in direct contact membrane distillation desalination, J. Membr. Sci., 433 (2013) 160–166.
[14] X. Yang, H. Yu, R. Wang, A.G. Fane, Analysis of the effect of turbulence promoters in hollow fiber membrane distillation modules by computational fluid dynamic (CFD) simulations, J. Membr. Sci., 415–416 (2012) 758–769.
[15] J. Phattaranawik, R. Jiraratananon, A.G. Fane, Heat transport and membrane distillation coefficients in direct contact membrane distillation, J. Membr. Sci., 212 (2003) 177–193.
[16] F.A. Banat, J. Simandl, Membrane distillation for dilute ethanol separation from aqueous streams, J. Membr. Sci., 163 (1999) 333–348.
[17] G.L. Liu, C. Zhu, C.S. Cheung, C.W. Leung, Theoretical and experimental studies on air gap membrane distillation, Heat Mass Transfer, 34 (1998) 329–335.
[18] S. Bouguecha, R. Chouikh, M. Dhahbi, Numerical study of the coupled heat and mass transfer in membrane distillation, Desalination, 152 (2003) 245–252.
[19] J.R. Welty, C.E. Wick, R.E. Wilson, Fundamentals of Momentum, Heat and Mass Transfer, 3rd ed., John Wiley & Sons, New York, 1984, pp. 169–176.
[20] S.G. Kandlikar, D. Schmitt, A.L. Carrano, J.B. Taylor, Characterization of surface roughness effects on pressure drop in single-phase flow in mini channels, Phys. Fluids, 17 (2005) 100606.
[21] U. Dehesa-Carrasco, C.A. Perez-Rabago, C.A. Arancibia-Bulnes, Experimental evaluation and modeling of internal temperatures in an air gap membrane distillation unit, Desalination, 326 (2013) 47–54.
[22] M. Essalhi, M. Khayet, Application of a porous composite hydrophobic/hydrophilic membrane in desalination by air gap and liquid gap membrane distillation: a comparative study, Sep. Purif. Technol., 133 (2014) 176–186.